ChemComm

COMMUNICATION

View Article Online
View Journal

Cite this: DOI: 10.1039/d0cc08084e

Received 13th December 2020,
Accepted 29th January 2021

DOI: 10.1039/d0cc08084e

rsc.li/chemcomm

Boron-modulated surface of hollow nickel framework for improved hydrogen evolution†

Weishi Gu,‡[a] Zhongqin Pan,‡[ab] Han Tao,[c] Yanling Guo,[a] Jun Pu,[d] Chenglin Zhong,[e] Jiachen Li,*[f] Changqing Ye*[a] and Qingwen Zhou*[a]

A hollow Ni framework (HNF) is designed and prepared to utilize the exterior and interior surface active sites of a Ni-based binder-free and support-free electrode. Furthermore, the more efficient Ni–B active sites are then *in situ* introduced on the surface of HNF. This micro/nano structure engineering, together with the surface boron modulation, results in a synergistically enhanced catalytic effect for the HER performance.

Hydrogen, as a clean and renewable energy source, could reduce our dependence on fossil fuels, curb CO_2 emission, and prevent global warming.[1] Electrochemical water splitting is an important and clean route to produce hydrogen. The hydrogen evolution reaction (HER) can be promoted by noble metal electrocatalysts like Pt. Non-precious metal catalysts usually show low activities and efficiencies. However, the scarcity and high cost of noble metals hamper their wide-spread applications. In this regard, exploring highly active and earth-abundant electrocatalysts has become a key task in the development of the hydrogen energy economy.

Ni has been considered as a promising candidate for HER electrocatalysis and is widely used in industrial alkaline water electrolysis, due to its good electroactive properties and excellent corrosion resistance in alkaline solutions.[2–4] In fact, Ni is a crucial component of hydrogen catalytic bioenzymes (such as [NiFe] hydrogenases) in nature.[5] To further improve the catalytic HER performance of Ni, great efforts have been invested in enriching or optimizing the surface active sites through the modulations of morphology, constituent compositions, and/or dopants.[6–8] For example, Xu *et al.* designed a 3D ordered macro-/mesoporous inverse opal structure to expand the active area of Ni nanoparticles, so as to improve the HER catalytic performance.[7] However, most of the reported Ni-based catalysts are in the form of powders, and thus they should be fabricated onto the current collector by introducing polymer binders (such as Nafion) to obtain the electrode. The difficulty with this strategy lies in the reduced charge transfer efficiency, poor ion diffusion, and weak physical contact.[9] Zhang *et al.* proposed an *in situ* process to construct Ni–P on the surface of an ordered porous Ni network electrodeposited on a Ni substrate.[8] The new active sites of Ni–P remarkably improved the HER activity of pure Ni in the binder-free electrode. However, the electrochemically active area will be inevitably limited due to the solid internal structure of the Ni network and Ni substrate. Thus, the utilization rate of Ni is low and any further improvement in the catalytic performance is hindered. This condition still remains an open question as to how to synergistically enrich and optimize the active sites both inside and on the surface of Ni, especially for binder-free electrodes.

Recently, transition-metal borides have attracted enormous attention on account of many attractive characteristics, including low cost, low over-potential, bifunctionality, and superior stability.[10] Amongst the candidates, nickel boride (Ni–B) is an earth-abundant transition metal alloy with good ductility and corrosion resistance.[11] Moreover, Ni–B has been found to have abundant active sites and highly electrocatalytic activities that enable efficient hydrogen production by water electrolysis.[12–15]

Inspired by this understanding, herein, we designed a boron-modulated HNF as both an electrode substrate and catalyst by itself. As shown in the schematic in Fig. 1, a porous

[a] *Institute of Environmental Health & Green Chemistry, School of Public Health, Nantong University, Jiangsu 226019, China. E-mail: qw_zhou@ntu.edu.cn, cqye@ntu.edu.cn*
[b] *State Key Laboratory of Analytical Chemistry for Life Sciences, School of Chemistry and Chemical Engineering, Nanjing University, Jiangsu 210023, China*
[c] *High School Affiliated To Nantong University, Jiangsu 226019, China*
[d] *Key Laboratory of Functional Molecular Solids (Ministry of Education), College of Chemistry and Materials Science, Anhui Provincial Engineering Laboratory for New-Energy Vehicle Battery Energy-Storage Materials, Anhui Normal University, Wuhu 241000, China*
[e] *College of Chemistry and Chemical Engineering, Linyi University, Linyi 276005, Shandong, China*
[f] *School of Chemical Engineering, Northwest University, Shaanxi 710069, China. E-mail: jiachen_li@nwu.edu.cn*

† Electronic supplementary information (ESI) available. See DOI: 10.1039/d0cc08084e

‡ These authors contributed equally to this work.

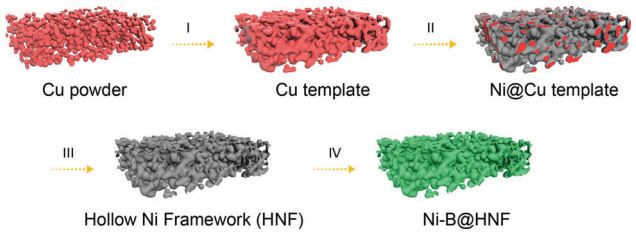

Fig. 1 Schematic illustration of the formation process of Ni-B@HNF: (I) preparation of Cu template by sintering Cu powder; (II) electroplating of a conformal nickel coating onto the surface of the Cu template; (III) etching of Cu to produce HNF; and (IV) boron-modulated surface of HNF to produce Ni-B@HNF.

metallic template was first prepared by slurry-casting copper powder (Fig. S1, ESI†) on a graphite plate and sintering in forming gas (5% H_2 and 95% Ar). Then, a conformal nickel coating was electroplated onto the internal surface of the copper template (Fig. S2a, ESI†). Etching of copper produced the HNF (Fig. S2b, ESI†), wherein a metallic nickel wall separates the space into two interconnected parts and thereby forms exterior and interior surfaces. HNF exhibits a much higher specific surface area than that of commercial Ni foam (NF) (Fig. S3, ESI†). Afterwards, the HNF was chemically boronized in an alkaline $NaBH_4$ solution to generate amorphous Ni–B, just like wearing a piece of gauze on the surfaces of HNF. Such a binder-free and support-free Ni-based electrode (Ni-B@HNF, Fig. S2c, ESI†) not only inherits advantages of the interconnected metallic scaffold expanding the active area and providing continuous and efficient electron/ion pathways, but also introduces the highly active sites of Ni–B, resulting in a synergistically enhanced catalytic effect for the HER performance.

The typical surface morphology of the samples is analysed by scanning electron microscopy (SEM). As can be seen in Fig. 2a and b, the obtained Ni-B@HNF has a highly porous and interconnected structure. The formation of this co-continuous structure is due to the sintering necks of Cu powder (Fig. S4, ESI†) and subsequent conformal deposition of Ni. The wall thickness of the hollow structure is around 100 nm (Fig. 2c). A cross-sectional SEM image of the monolithic electrode shows that the vertical thickness is around 100 μm (Fig. S5, ESI†). No apparent differences in morphology are observed for Ni-B@HNF and HNF (Fig. S6, ESI†), which expedites direct comparison of their electrocatalytic HER activities.

The energy dispersive X-ray (EDX) spectroscopy and elemental mapping images of Ni-B@HNF confirm that Ni, O, and B are uniformly distributed throughout the entire sample (Fig. 2d). The inductively coupled plasma atomic emission spectroscopy (ICP-AES) analysis reveals that B is ~0.05 wt% in Ni-B@HNF. The crystalline phase of Ni-B@HNF characterized by X-ray diffraction (XRD) is shown in Fig. S7 (ESI†). No remarkable diffraction peaks are observed for Ni-B@HNF except for the parent Ni, implying the formation of a thin-layer of amorphous Ni–B on the surface of HNF. The transmission electron microscopy (TEM) image also shows that Ni-B@HNF has an additional thin-layer of Ni–B on the surface of Ni (Fig. S8, ESI†). Selected area electron diffraction (SAED) of Ni-B@HNF displays several diffraction rings, which can be attributed to the lattice fringes of the (111) and (220) planes of Ni (Fig. S9, ESI†). No other specific rings in the SAED pattern further confirms the amorphous nature of Ni–B in Ni-B@HNF. To understand the electronic structures of Ni–B originating from HNF, X-ray photoelectron spectroscopy (XPS) is performed on Ni-B@HNF and HNF. The Cu element is not detected in Ni-B@HNF while the Ni@Cu template shows obvious Cu signals, indicating the complete removal of the Cu template during chemical etching (Fig. S10 and Table S1, ESI†). As depicted in Fig. 3a, the Ni $2p_{1/2}$ core level in the XPS spectra displays a Ni^0 peak at 852.5 eV on the surface of HNF with a strong Ni^{2+} peak at 855.6 eV.[9,16] The relatively high Ni^{2+} species in HNF could be attributed to the oxidation of metal Ni during the copper etching in a concentrated alkaline solution containing strong oxidising agents.[17,18] This result is also consistent with the EDX elemental mapping of HNF (Fig. S6d, ESI†). After chemical-boronation, the signal of Ni^0 positively shifts to higher binding energy at 852.7 eV, which is assigned to the low valence of $Ni^{\delta+}$ ($0 \leq \delta < 2$), implying a

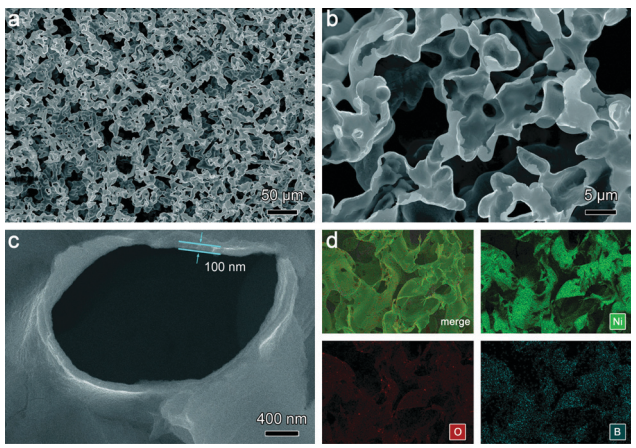

Fig. 2 SEM images of (a–c) the Ni-B@HNF at different magnifications, and (d) EDX elemental mapping images of Ni, O, and B for the Ni-B@HNF.

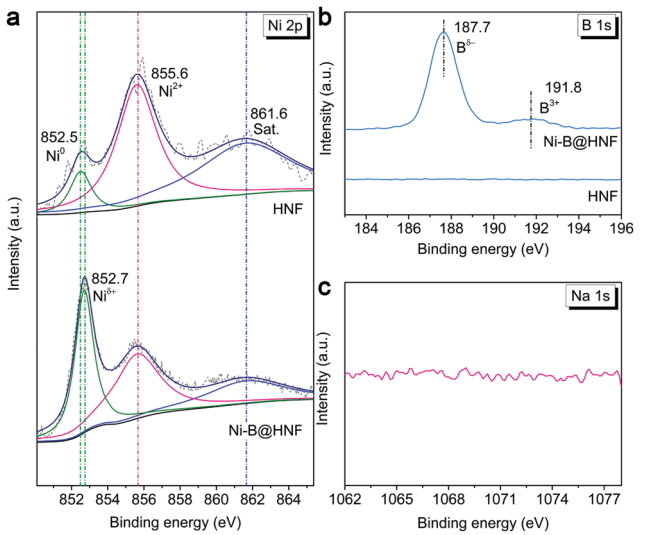

Fig. 3 XPS spectra of HNF and Ni-B@NHF: (a) Ni 2p, (b) B 1s, and (c) Na 1s.

changing chemical environment with the boronation of the surface Ni.[14,19] The reduced peak intensity of Ni^{2+} further evidences the occurrence of reduction or boronization reactions around the surface of HNF. Fig. 3b shows that the B 1s of Ni-B@HNF has two peaks at 187.7 and 191.8 eV, corresponding to borides and oxidized boron species arising from superficial oxidation,[20,21] respectively. Other elements including Na (Fig. 3c) and B (Fig. 3b) are not detected in Ni-B@HNF and HNF, respectively, suggesting that no residual Na is found in the as-prepared Ni-B@HNF, and thus only B is incorporated into Ni during the synthesis. The B 1s peak is negatively shifted by 0.2 eV compared to reference peaks of elemental B (187.9 eV).[22] The XPS analysis of Ni 2p and B 1s not only shows the characters of Ni–B active species, but also exhibits strong electron interactions between Ni and B, in which the electrons are transferred from Ni to B, resulting in partially positive charge (δ^+) in Ni and partially negative charge (δ^-) in B. According to previous research,[12,14] such transfer between Ni and B is considered to be in favour of improving the HER activity.

To assess the HER electrocatalytic activity of Ni-B@HNF, all electrochemical measurements were performed in a 1.0 M KOH solution using a typical three-electrode system. For comparison, NF, HNF, and commercial 20 wt% Pt/C coated on HNF (denoted as Pt/C@HNF) are also evaluated. As clearly shown in Fig. 4a, NF also shows a certain HER performance due to the nature of Ni. NF requires an overpotential of 220 mV (η_{10}) at -10 mA cm^{-2} and 481 mV (η_{100}) at -100 mA cm^{-2}. Obviously, HNF shows a great improvement of HER performance (η_{10} = 122 mV, η_{100} = 336 mV), emphasizing the significance of morphology modulations for pure Ni. More interestingly, Ni-B@HNF just needs 83 (η_{10}) and 185 mV (η_{100}) to reach the same current densities. Moreover, at an overpotential of 213 mV, the current density (j_{213}) of Ni-B@HNF reaches -200 mA cm^{-2}, which is $\sim$5.3 times that of HNF (-37.6 mA cm^{-2}). The mass-normalized LSV curves are illustrated in Fig. S11 (ESI†), showing the same activity trend.

In order to figure out the detailed reasons for this substantial improvement, the electrochemical surface area (ECSA) of different electrodes is further investigated. The ESCA characterizes the efficient area involved in the HER and can be determined by measuring the non-faradaic electrical double-layer capacitance (C_{dl})[23,24] (Fig. S12 and S13, ESI†). The value of C_{dl} is linearly proportional to ECSA. The C_{dl} of Ni-B@HNF (2.59 mF cm^{-2}) is very close to that of HNF (2.46 mF cm^{-2}) (Fig. 4b). This result is consistent with the SEM analyses. In that case, the 5.3-fold activity enhancement of Ni-B@HNF originates from the newly introduced active sites to a greater extent, rather than ECSA. In addition, the HER activities of the as-prepared Ni-B@HNF electrodes with different amounts of boronization time show that the optimal condition is 2 min with a boron mass fraction of 0.05 wt% (Fig. S14 and Table S2, ESI†). Surprisingly, Ni-B@HNF exhibits even higher activity than commercial Pt/C when the overpotential is beyond 208 mV (Fig. 4a). The HER activity of Ni-B@HNF is also compared with that of the previously reported electrocatalysts and it performs better than most Ni-based binder-free electrodes (Table S3, ESI†).

The Tafel slope is determined to evaluate the HER kinetics. As shown in Fig. 5a, the measured Tafel slope for Pt/C@HNF is about 63 mV dec^{-1}, close to the literature values.[25] The Tafel slope of HNF is around 117 mV dec^{-1}, which is further decreased to 94 mV dec^{-1} for Ni-B@HNF. This suggests the enhanced HER kinetics because of B modulation, further explaining the improvement of HER performance. Such difference is generally related to the initial water dissociation and the different adsorption for H*, although both of them probably follow the same Volmer–Heyrovsky mechanism according to the Tafel slope[8,26,27] (see Note S1, ESI†). The fast electrode reaction kinetics of Ni-B@HNF is made more evident by electrochemical impedance spectroscopy (EIS). Fig. 5b shows the Nyquist plots of HNF and Ni-B@HNF at the overpotential of 100 mV. The Nyquist plots are fitted with an equivalent circuit (Fig. S15, ESI†). Ni-B@HNF has a charge transfer resistance (R_{ct}) of $\approx$ 0.82 Ω, which is much lower than that of HNF ($\approx$ 1.71 Ω). It indicates that the B modulation enhances the charge transport kinetics of the catalytic HER.[28]

Yet another important criterion for an HER electrode is its operational stability. The stability of Ni-B@HNF is first evaluated by comparing the HER polarization curves tested before and after 3000 cyclic voltammogram (CV) cycles (Fig. 5c). The overpotentials for Ni-B@HNF can be well maintained with only a negligible loss of $\approx$ 6 mV at -10 mA cm^{-2} after the CV sweeps. The HER stability is

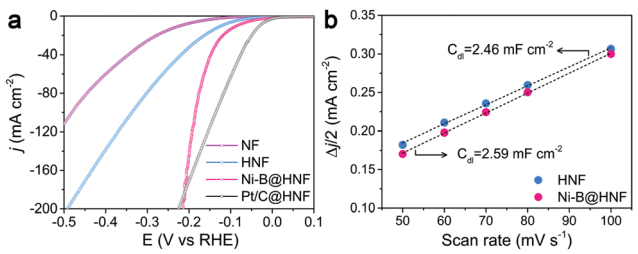

Fig. 4 (a) HER polarization curves and (b) double layer capacitive currents *vs.* scan rates of the electrodes.

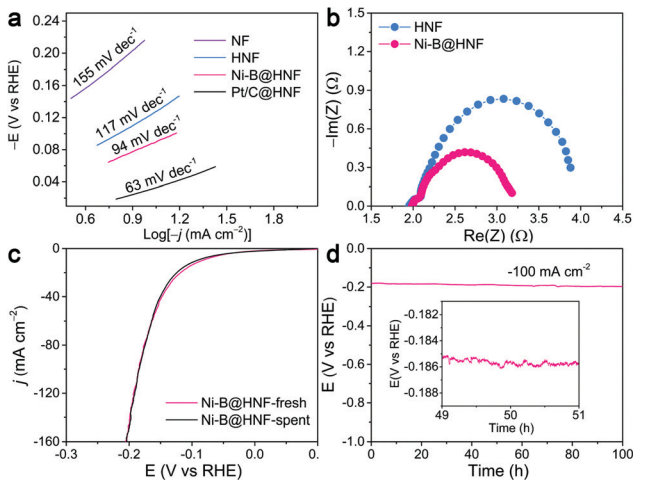

Fig. 5 (a) Tafel and (b) Nyquist plots of the electrodes. (c) HER polarization curves of Ni-B@HNF before and after 3000 continuous CV cycles. (d) Long-term stability tests of Ni-B@HNF at the current density of -100 mA cm^{-2}. The inset shows the expanded curve parts with oscillations.

then investigated by chronopotentiometry and the result is illustrated in Fig. 5d. During the galvanostatic electrolysis at -100 mA cm^{-2}, the overpotentials only increase to $\approx$ 15 mV after 100 h. Moreover, there are no significant morphological changes after the long-term electrolysis (Fig. S16, ESI†). XRD, XPS, and ICP characterizations after the stability test verify no obvious changes in the crystalline structure, valence state and composition (Fig. S17, S18 and Table S4, ESI†). The amount of produced H_2 is calculated *via* gas chromatography and a near unity faradaic efficiency is obtained. The signal fluctuations of the expanded chronopotentiometric curve also imply the formation and release of H_2 bubbles on the surface of Ni-B@HNF (Fig. 5d inset). All of these results manifest that Ni-B@HNF possesses excellent operational stability even under a high current density, which is advantageous for practical applications.

In summary, we develop a novel approach to fabricate Ni-based electrodes with exterior-interiorly exposed and boronized surfaces by preferentially dissolving a less stable metal phase from a conformal two-phase precursor and subsequent *in situ* boron modulation. Advantageously, the obtained Ni framework possesses a hollow and interconnected micro/nano structure, with a piece of boron-modulated "gauze" on its surfaces, and works as both substrate and catalyst by itself, endowing the monolithic electrode with binder-free and support-free features. Thus, the active sites both inside and on the surface of Ni can be synergistically enriched and optimized, making our system different from other invested efforts as to how to improve the catalytic HER performance of Ni. More interestingly, the resultant electrode displays favourable HER performance with an overpotential of 83 mV to achieve -10 mA cm^{-2}, and surpasses Pt/C at large current density, along with impressive stability. Overall, we demonstrate that the micro/nano structure engineering, together with the surface boron modulation, successfully realize an enhanced HER performance of Ni and presents a new technique for monolithic electrode fabrication.

This work is financially supported by the Research Fund of Nantong University (No. 03083036), the Nantong Science and Technology Planned Project (No. MS12019044), the National Natural Science Foundation for Young Scholars of China (No. 52002189), the Natural Science Foundation for Young Scholars of Jiangsu Province, China (No. BK20200979), the Natural Science Research Projects of Universities in Jiangsu Province (No. 20KJB430035), and the Postdoctoral Science Foundation of China (No. 2019M663945XB).

Conflicts of interest

There are no conflicts to declare.

Notes and references

1 X. Zou and Y. Zhang, *Chem. Soc. Rev.*, 2015, **44**, 5148–5180.
2 V. D. Jović, B. M. Jović, U. Č. Lačnjevac, N. V. Krstajić, P. Zabinski and N. R. Elezović, *J. Electroanal. Chem.*, 2018, **819**, 16–25.
3 L. Ji, C. Lv, Z. Chen, Z. Huang and C. Zhang, *Adv. Mater.*, 2018, **30**, 1705653.
4 R. Subbaraman, D. Tripkovic, D. Strmcnik, K.-C. Chang, M. Uchimura, A. P. Paulikas, V. Stamenkovic and N. M. Markovic, *Science*, 2011, **334**, 1256–1260.
5 P. Liu and J. A. Rodriguez, *J. Am. Chem. Soc.*, 2005, **127**, 14871–14878.
6 C. Hu, Q. Ma, S.-F. Hung, Z.-N. Chen, D. Ou, B. Ren, H. M. Chen, G. Fu and N. Zheng, *Chemistry*, 2017, **3**, 122–133.
7 T. Sun, C. Zhang, J. Chen, Y. Yan, A. A. Zakhidov, R. H. Baughman and L. Xu, *J. Mater. Chem. A*, 2015, **3**, 11367–11375.
8 K. Xiong, Y. Gao, J. Chen, Y. Shen and H. Zhang, *Chem. Commun.*, 2020, **56**, 611–614.
9 J. Li, H. Chen, Y. Liu, R. Gao and X. Zou, *J. Mater. Chem. A*, 2019, **7**, 5288–5294.
10 J. Masa, P. Weide, D. Peeters, I. Sinev, W. Xia, Z. Sun, C. Somsen, M. Muhler and W. Schuhmann, *Adv. Energy Mater.*, 2016, **6**, 1502313.
11 W. Yuan, X. Zhao, W. Hao, J. Li, L. Wang, X. Ma and Y. Guo, *ChemElectroChem*, 2019, **6**, 764–770.
12 H. Xu, B. Fei, G. Cai, Y. Ha, J. Liu, H. Jia, J. Zhang, M. Liu and R. Wu, *Adv. Energy Mater.*, 2020, **10**, 1902714.
13 X. Xu, Y. Deng, M. Gu, B. Sun, Z. Liang, Y. Xue, Y. Guo, J. Tian and H. Cui, *Appl. Surf. Sci.*, 2019, **470**, 591–595.
14 T. Huang, T. Shen, M. Gong, S. Deng, C. Lai, X. Liu, T. Zhao, L. Teng and D. Wang, *Chin. J. Catal.*, 2019, **40**, 1867–1873.
15 C. Adán, F. J. Pérez-Alonso, S. Rojas, M. A. Peña and J. L. G. Fierro, *Int. J. Hydrogen Energy*, 2012, **37**, 14984–14991.
16 W.-K. Choi, S. Guo Zhang, J.-I. Murayama, R. Shinya, H. Inoue and C. Iwakura, *J. Alloys Compd.*, 1998, **280**, 99–103.
17 Q. Kong, W. Feng, Q. Zhang, P. Zhang, Y. Sun, Y. Yin, Q. Wang and C. Sun, *ChemCatChem*, 2019, **11**, 3004–3009.
18 X. Wei, Y. Li, L. Chen and J. Shi, *Angew. Chem., Int. Ed.*, 2021, **60**, 3148–3155.
19 Y. N. Bekish, T. V. Gaevskaya, L. S. Tsybulskaya, G.-Y. Lee and M. Kim, *Prot. Met. Phys. Chem. Surf.*, 2010, **46**, 325–331.
20 W.-J. Jiang, S. Niu, T. Tang, Q.-H. Zhang, X.-Z. Liu, Y. Zhang, Y.-Y. Chen, J.-H. Li, L. Gu, L.-J. Wan and J.-S. Hu, *Angew. Chem., Int. Ed.*, 2017, **56**, 6572–6577.
21 Q. Hu, G. Li, Z. Han, Z. Wang, X. Huang, X. Chai, Q. Zhang, J. Liu and C. He, *Adv. Energy Mater.*, 2019, **9**, 1901130.
22 C. Ronning, D. Schwen, S. Eyhusen, U. Vetter and H. Hofsäss, *Surf. Coat. Technol.*, 2002, **158–159**, 382–387.
23 D. Li, Z. Pan, H. Tao, J. Li, W. Gu, B. Li, C. Zhong, Q. Jiang, C. Ye and Q. Zhou, *Chem. Commun.*, 2020, **56**, 12399–12402.
24 X. Liang, L. Shi, R. Cao, G. Wan, W. Yan, H. Chen, Y. Liu and X. Zou, *Adv. Mater.*, 2020, **32**, 2001430.
25 W. Hao, R. Wu, R. Zhang, Y. Ha, Z. Chen, L. Wang, Y. Yang, X. Ma, D. Sun, F. Fang and Y. Guo, *Adv. Energy Mater.*, 2018, **8**, 1801372.
26 H. Sun, Z. Ma, Y. Qiu, H. Liu and G.-G. Gao, *Small*, 2018, **14**, 1800294.
27 X. Ji, Y. Zhang, Z. Ma and Y. Qiu, *ChemSusChem*, 2020, **13**, 5004–5014.
28 X. Long, G. Li, Z. Wang, H. Zhu, T. Zhang, S. Xiao, W. Guo and S. Yang, *J. Am. Chem. Soc.*, 2015, **137**, 11900–11903.

